

SG-LRA: Self-Generating Automatic Scoliosis Cobb Angle Measurement with Low-Rank Approximation

Zhiwen Shao, Yichen Yuan, Lizhuang Ma, Dit-Yan Yeung, and Xiaoja Zhu

Abstract—Automatic Cobb angle measurement from X-ray images is crucial for scoliosis screening and diagnosis. However, most existing regression-based methods and segmentation-based methods struggle with inaccurate spine representations or mask connectivity/fragmentation issues. Besides, landmark-based methods suffer from insufficient training data and annotations. To address these challenges, we propose a novel framework including Self-Generation pipeline and Low-Rank Approximation representation (SG-LRA) for automatic Cobb angle measurement. Specifically, we propose a parameterized spine contour representation based on LRA, which enables eigen-spine decomposition and spine contour reconstruction. We can directly obtain spine contour with only regressed LRA coefficients, which form a more accurate spine representation than rectangular boxes. Also, we combine LRA coefficient regression with anchor box classification to solve inaccurate predictions and mask connectivity issues. Moreover, we develop a data engine with automatic annotation and automatic selection in an iterative manner, which is trained on a private Spinal2023 dataset. With our data engine, we generate the largest scoliosis X-ray dataset named

Spinal-AI2024 largely without privacy leaks. Extensive experiments on public AASCE2019, private Spinal2023, and generated Spinal-AI2024 datasets demonstrate that our method achieves state-of-the-art Cobb angle measurement performance. Our code and Spinal-AI2024 dataset are available at <https://github.com/Ernestchenchen/SG-LRA> and <https://github.com/Ernestchenchen/Spinal-AI2024>, respectively.

Index Terms—Automatic Cobb angle measurement, self-generation pipeline, low-rank approximation representation, largest scoliosis X-ray dataset

I. INTRODUCTION

SCOLIOSIS is an important spinal disease in human beings, especially for Scoliosis, a common spinal deformity that primarily affects adolescents, can significantly impact the health of patients [1], [2], [3]. Early detection and treatment of scoliosis can help reduce the need for surgical interventions [4]. The Cobb angle [5] is one of the most widely used clinical measures for evaluating and diagnosing the severity of scoliosis. It is defined as the angle between parallel lines of the top of the upper end vertebra (the most tilted vertebrae on the curve) and the bottom of the lower one [6]. There are three regional spinal deformities associated with different spinal segments: proximal thoracic (PT), main thoracic (MT), and thoracolumbar/lumbar (TL/L), as illustrated in Fig. 1(c).

Currently, manual Cobb angle measurement on radiographic images like X-ray images by experts is still the mainstream way in medical institutions. However, it is time-consuming and often has potential errors [7], [8], since it can be affected by spinal selection and inter-observer variability, which can be observed from the distances between manual angles and angles by landmarks in Fig. 1(a). It has been validated that manual annotation of the Cobb angle exhibits fluctuations ranging from 2.8 to 8 degrees [9]. Therefore, developing a reliable automatic Cobb angle measurement method is crucial.

Traditional automatic Cobb angle measurement methods rely on hand-crafted features [10], [11], limiting model performance and generalization. In recent years, some regression-based methods use rectangular boxes as the spine representation [12], [13], which suffer from reduced accuracy when spinal blocks are wedge-shaped or irregular, as shown in Fig. 1(a). Segmentation-based methods are sensitive to image quality [14], [15], tending to predict connected or damaged spinal masks for low-quality inputs. Landmark-based methods

Manuscript received November, 2024. This work was supported in part by the National Natural Science Foundation of China under Grants 62472424 and 62106268, in part by the China Postdoctoral Science Foundation under Grant 2023M732223, and in part by the Hong Kong Scholars Program under Grant XJ2023037. It was also supported in part by the National Natural Science Foundation of China under Grant 72192821, and in part by the Joint Fund for Medical Artificial Intelligence under Grant MAI2023Q022. (Corresponding authors: Yichen Yuan, Dit-Yan Yeung, and Xiaoja Zhu.)

This work involved human subjects in its research. All ethical and experimental procedures and protocols was approved by the Medical Research Ethics Committee of The First Affiliated Hospital of USTC under Grant 2023KY-370.

Z. Shao and Y. Yuan are with the School of Computer Science and Technology, China University of Mining and Technology, Xuzhou 221116, China, and also with the Mine Digitization Engineering Research Center of the Ministry of Education, Xuzhou 221116, China. Z. Shao is also with the Department of Computer Science and Engineering, Hong Kong University of Science and Technology, Clear Water Bay, Kowloon 999077, Hong Kong, and also with the Department of Computer Science and Engineering, Shanghai Jiao Tong University, Shanghai 200240, China (e-mail: {zhiwen_shao; yuanyichen}@cumt.edu.cn).

L. Ma is with the Department of Computer Science and Engineering, Shanghai Jiao Tong University, Shanghai 200240, China (e-mail: maz@cs.sjtu.edu.cn).

D.-Y. Yeung is with the Department of Computer Science and Engineering, Hong Kong University of Science and Technology, Clear Water Bay, Kowloon 999077, Hong Kong (e-mail: dyyeung@cse.ust.hk).

X. Zhu is with the Xuzhou Central Hospital/The Xuzhou Clinical School of Xuzhou Medical University, Xuzhou 221009, China, and also with the Department of Orthopedics, The First Affiliated Hospital of USTC, Division of Life Sciences and Medicine, University of Science and Technology of China, Hefei 230001, China (e-mail: xiaoja_zhu@foxmail.com).

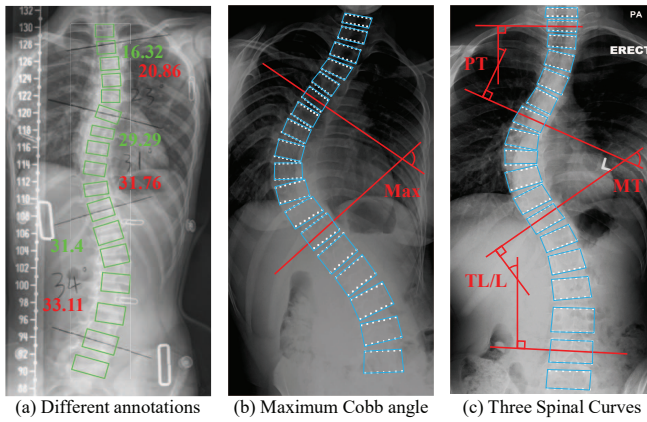


Fig. 1. Illustration of Cobb angle measurement. There are three categories of scoliosis: proximal thoracic (PT) curve, main thoracic (MT) curve, and thoracolumbar/lumbar (TL/L) curve, as shown in (c). In (a), handwritten 23° , 31° , and 34° are manually measured by experts, angles in green are measured based on rectangular boxes (also in green), and angles in red are measured based on our proposed contour boxes composed by spinal landmarks (drawn in (b)). (b) and (c) show two types of evaluations: maximum angle of three spinal curves, three regional angles, respectively.

necessitate vast amounts of training data and annotations [16], [17], [18], which are costly and time-consuming to collect and label, and are exacerbated by data scarcity due to patient privacy concerns.

In this paper, we distill the above limitations as three main issues, and tackle them from three aspects: (a) How to achieve more accurate spine representation? (b) How to generate sufficient scoliosis images while protecting patient privacy? (c) How to obtain accurate annotations at low costs?

Parameterized Spine Representation. We propose a novel automatic Cobb angle measurement framework named SG-LRA. We combine regression-based and landmark-based techniques, by using a set of spinal landmarks to represent the bounding box of spinal segments. Inspired by low-rank approximation (LRA) parameterized contour representation in object detection [19], [20], we use LRA to learn eigenspines from spine contours of training data, and reconstruct spine contours via LRA coefficients. To suppress inaccurate predictions and mask connectivity, we integrate LRA coefficient regression with anchor box classification to obtain spinal segment contours, in which sparse and dense assignments are integrated to more precisely detect spinal segments.

Privacy-Preserving Scoliosis Generation. We explore the latent diffusion model (LDM) [21] for scoliosis image synthesis. Specifically, we train LDM on our private dataset Spinal2023, utilizing a diffusion process to map raw images from pixel to latent space. During inference, the trained LDM with text-conditioned prompts can generate X-ray images. To mitigate privacy leaks [22], we employ data augmentation during LDM training, promote data balance, and introduce a privacy review [23] to exclude potentially privacy-compromising samples based on structural and pixel similarities, coupled with manual verification.

Cost-Effective Semi-Supervised Annotation. Inspired from semi-supervised pseudo-labeling [24] and multi-stage interactive annotation [25], we propose a new data engine, which

drives an iterative pipeline with automatic annotation and selection. It consists of four stages: pseudo-labeling, auto-annotation, manual-assisted annotation, and privacy review. At each iteration, spine contour detection network is first re-trained using current dataset, and its trained model is used for pseudo-labeling so as to further update the dataset. This iterative pipeline culminates in our open-source dataset named Spinal-AI2024, which is the largest scoliosis X-ray dataset.

The main contributions of this paper are threefold:

- We propose a novel low-rank approximation parameterized spine representation for automatic Cobb angle measurement, in which LRA coefficient regression and anchor box classification with sparse and dense assignments are combined to detect irregular contours of spinal segments.
- We propose a new data engine with semi-supervised labeling and privacy review in an iterative manner, which enables the generation of large-scale scoliosis X-ray images largely without privacy leaks. To our knowledge, our open-source Spinal-AI2024 is the largest scoliosis X-ray dataset.
- Extensive experiments on AASCE2019, Spinal2023, and Spinal-AI2024 datasets show that our method outperforms state-of-the-art automatic Cobb angle measurement works for both maximum angle and three regional angles.

II. RELATED WORK

A. Scoliosis Cobb Angle Measurement

Earlier methods [10], [11], [26], [27] adopt traditional machine learning to approximate the relationship between image features and Cobb angles. However, these methods suffer from performance and generalization issues due to loss of high-resolution details through downsampling [17] or reliance on hand-crafted features. Recently, deep learning based methods [28], [29] have gained increasing attention.

Regression-based methods [12], [13], [27], [30] aim to learn a direct mapping between the spinal shape representation and the Cobb angle, without explicit geometric calculations. However, these approaches have limited performance for wedge-shaped or irregular vertebrae due to rectangular shape assumption.

Segmentation-based methods [14], [31], [32] usually rely on U-Net [33] or its modifications [34], [15], by performing pixel-level classification and then combining pixels as spinal regions. However, these methods are sensitive to image quality, and often require pre-processing to address noise, resolution, and contrast issues [35], [32].

Landmark-based methods [36], [16], [37], [17], [38] focus on localizing spinal landmarks, which often requires vast training data. In this paper, we overcome the data scarcity issue by predicting landmarks through LRA coefficient regression, leveraging our proposed data engine with automatic annotation and selection.

B. Medical Image Generation

Deep learning relies heavily on numerous labeled training data [39]. In the medical image field, there is often a scarcity

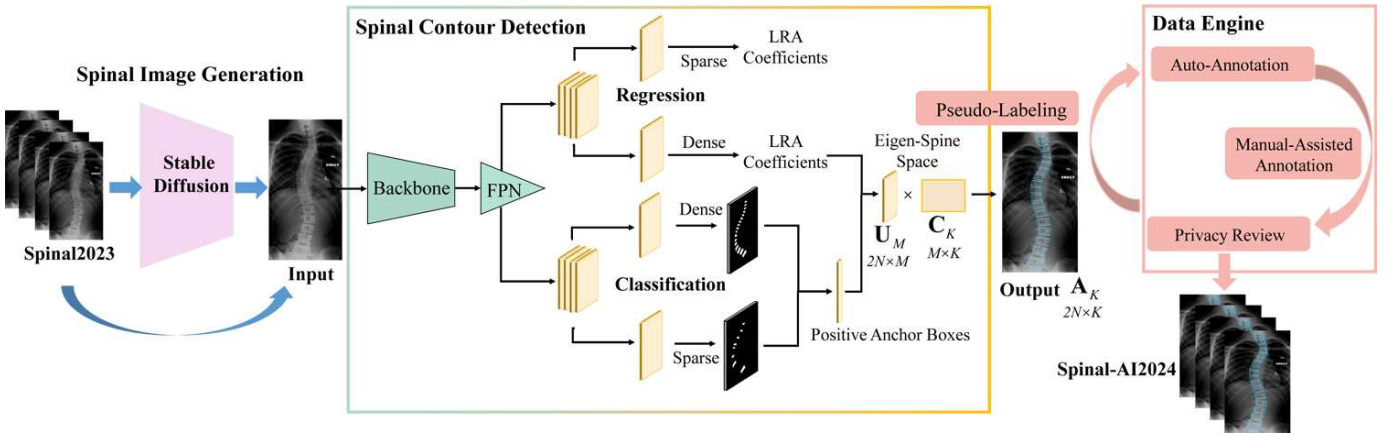


Fig. 2. The overall structure of our SG-LRA framework, which consists of spinal image generation, spinal contour detection, and data engine. Our private Spinal2023 dataset is used for training spinal image generation model, and also used for training initial model of spinal contour detection network. During each round of data engine, trained spinal contour detection network is adopted for pseudo-labeling, and selected data with annotations are backward used to fine-tune the spinal contour detection network. By employing the data engine to select and annotate generated images, we obtain the Spinal-AI2024 dataset.

of annotated data due to cumbersome, time-consuming, and expensive image acquisition and annotation [40]. To alleviate this limitation, previous works use data perturbation [41] or data synthesis [42].

Generative models like generative adversarial networks (GANs) [43], [44] have demonstrated the capability to produce realistic, high-resolution images [44], [45], [46], [47]. Recent studies [22] indicate that diffusion models [21] possess higher generation capacity than GANs. Packhäuser *et al.* [23] utilized LDM to generate chest X-ray images, and proposed a sampling strategy that safeguards the privacy of sensitive biometric information. However, sharing sensitive data under stringent privacy regulations remains a critical challenge in medical research [48], [49]. In this paper, we also leverage LDM to generate scoliosis X-ray images. Additionally, we propose a privacy-auditing module combined with pseudo-label training, utilizing a comprehensive privacy similarity mechanism to filter out images that may expose patient privacy.

C. Semi-Supervised Labeling

Semi-supervised labeling methods can be categorized into consistency regularization and pseudo-labeling approaches. Consistency regularization methods [50], [51] rely on modality-specific augmentation for regularization. Pseudo-labeling methods [52] predict labels for unlabeled data and train the model in a supervised manner.

Shi *et al.* [53] adopted local neighborhood density-based confidence scores to facilitate pseudo-labeling. Inspired by noise correction [54], Wang *et al.* [55] updated pseudo-labels by an optimization framework. Xie *et al.* [56] demonstrated the effectiveness of self-training in supervised classification tasks. However, these methods struggle with flawed pseudo-labels. Recently, Rizve *et al.* [24] selected high-quality pseudo-labels from noisy samples based on uncertainty. Kirillov *et al.* [25] built a data engine to augment data through manual-assisted, semi-automatic, and fully automatic phases. In this paper, we employ a similar semi-automatic annotation pipeline

to expand datasets, in which pseudo-label selection and manual assistance are integrated for quality improvement.

III. METHODOLOGY

The architecture of our framework is illustrated in Fig. 2. Given our private Spinal2023 dataset, we first train Stable Diffusion [21] to generate vast spinal X-ray images. Specifically, the generation starts from the original pixel space, undergoing diffusion. The textual condition and pixel features are then fed into the latent space, where cross-attention modules produce the final output.

Also, we use Spinal2023 to train an initial model of spinal contour detection network. This network adopts ResNet50 [57] as backbone, and uses feature pyramid network (FPN) [58] to extract multi-scale features. Then, it uses regression and classification branches to predict LRA coefficients and positive anchor boxes, respectively. In both branches, sparse and dense assignments are combined to improve the detection performance. Finally, we select LRA coefficients corresponding to positive anchor boxes to reconstruct spinal segment contours.

The data engine integrates a loop with a screening mechanism. The screening process encompasses pixel-level privacy checks, sample-level legality reviews, and segment-level quality assessments. At each iteration, spine contour detection network is fine-tuned using current data, and its trained model is further used for pseudo-labeling so as to update the data and annotations.

A. Spinal Contour Detection via LRA

1) *Parameterized Spine Representation*: To address inaccuracy of rectangular box based spine representation in prior works, we utilize contour box composed by spinal landmarks to represent spinal segments. Given that spinal segments generally exhibit similar structural properties and notable correlations among their contours, we develop a new parameterized spinal contour representation method based on such correlations from training data.

In particular, the boundary of a spinal segment is composed of N vertices, i.e. landmarks, which can be represented as a vector $\mathbf{a} = [x_1, y_1, \dots, x_N, y_N] \in \mathbb{R}^{2N \times 1}$ containing x and y coordinates. Then, we construct a spinal contour matrix $\mathbf{A} = [\mathbf{a}_1, \mathbf{a}_2, \dots, \mathbf{a}_L] \in \mathbb{R}^{2N \times L}$ from training data containing L spinal segment instances. Subsequently, we employ singular value decomposition (SVD) to extract the underlying structural relationship among \mathbf{A} :

$$\mathbf{A} = \mathbf{U}\mathbf{\Sigma}\mathbf{V}^T = \sigma_1 \mathbf{u}_1 \mathbf{v}_1^T + \dots + \sigma_r \mathbf{u}_r \mathbf{v}_r^T, \quad (1)$$

where $\mathbf{U} = [\mathbf{u}_1, \mathbf{u}_2, \dots, \mathbf{u}_{2N}] \in \mathbb{R}^{2N \times 2N}$ and $\mathbf{V} = [\mathbf{v}_1, \mathbf{v}_2, \dots, \mathbf{v}_L] \in \mathbb{R}^{L \times L}$ are orthogonal matrices. $\mathbf{\Sigma} \in \mathbb{R}^{2N \times L}$ is a diagonal matrix composed of singular values $\sigma_1 \geq \sigma_2 \geq \dots \geq \sigma_r > 0$, in which r is the rank of \mathbf{A} .

Each singular vector represents an orthogonal direction in the eigen-space. By retaining the first M singular values and their corresponding vectors while truncating the remaining low-rank components in Eq. (1), we can approximate \mathbf{A} as

$$\mathbf{A}_M = \sigma_1 \mathbf{u}_1 \mathbf{v}_1^T + \dots + \sigma_M \mathbf{u}_M \mathbf{v}_M^T = \mathbf{U}_M \mathbf{\Sigma}_M \mathbf{V}_M^T, \quad (2)$$

where \mathbf{A}_M is the best rank- M approximation of \mathbf{A} , since it minimizes the Frobenius norm $\|\mathbf{A} - \mathbf{A}_M\|_F$ [59].

Then, we define $\mathbf{C}_M = \mathbf{\Sigma}_M \mathbf{V}_M^T = [\mathbf{c}_1, \mathbf{c}_2, \dots, \mathbf{c}_L] \in \mathbb{R}^{M \times L}$, such that \mathbf{A}_M can be represented as

$$\mathbf{A}_M = [\mathbf{U}_M \mathbf{c}_1, \dots, \mathbf{U}_M \mathbf{c}_L] = [\tilde{\mathbf{a}}_1, \dots, \tilde{\mathbf{a}}_L], \quad (3)$$

where $\tilde{\mathbf{a}}_i = \mathbf{U}_M \mathbf{c}_i = [\mathbf{u}_1, \mathbf{u}_2, \dots, \mathbf{u}_M] \mathbf{c}_i$ is the approximation of \mathbf{a}_i . We refer to $\mathbf{u}_1, \dots, \mathbf{u}_M$ as *eigen-spines*, since they are eigen-vectors of the matrix $\mathbf{A}\mathbf{A}^T$ and can be viewed as principal spinal segment shapes.

For any $2N$ -dimensional spinal segment contour \mathbf{a} , we can project it onto the eigen-spine space:

$$\mathbf{c} = \mathbf{U}_M^T \mathbf{a}, \quad (4)$$

where $\mathbf{c} \in \mathbb{R}^{M \times 1}$ is the LRA coefficient vector.

2) Spinal Contour Detection Network: As shown in Fig. 2, our spinal contour detection network contains regression and classification branch, in which the overall loss is defined as

$$\mathcal{L} = \lambda_{reg} \mathcal{L}_{reg} + \lambda_{cls} \mathcal{L}_{cls}, \quad (5)$$

where \mathcal{L}_{reg} and \mathcal{L}_{cls} are the losses for the regression and classification branches, respectively, and λ_{reg} and λ_{cls} control their importances. \mathcal{L}_{cls} is composed by the spine region loss \mathcal{L}_{sr} in dense assignment and the sparse sampling region loss \mathcal{L}_{ssr} in sparse assignment:

$$\mathcal{L}_{cls} = \mathcal{L}_{sr} + \mathcal{L}_{ssr}, \quad (6)$$

in which \mathcal{L}_{sr} and \mathcal{L}_{ssr} use the form of cross-entropy loss and focal loss, respectively. \mathcal{L}_{reg} is defined as

$$\mathcal{L}_{reg} = \sum_i \mathbb{1}[i \in ps] l_1(\tilde{\mathbf{a}}_i, \mathbf{a}_i), \quad (7)$$

where l_1 denotes smooth-L1 loss, ps denotes the positive sample region obtained by incorporating sparse and dense assignments, and $\mathbb{1}$ denotes indicator function, outputting 1 when the condition is valid (the i -th point is within ps in Eq. (7)) and outputting 0 otherwise. After combining the

outputs of regression and classification branches, we can obtain a LRA coefficient matrix $\mathbf{C}_K \in \mathbb{R}^{M \times K}$. The predicted spinal segment locations are calculated as

$$\mathbf{A}_K = \mathbf{U}_M \mathbf{C}_K, \quad (8)$$

where K denotes the number of detected spinal segments.

Algorithm 1 The overall procedure of our data engine.

Input: Labeled dataset $D_{spinal2023}$, unlabeled dataset $D_{selected}$ generated by Stable Diffusion, sample selection index set $V_{selected}$ initialized as empty set, and spinal contour detection network with parameters Θ .

Output: Labeled dataset $D_{SpinalAI2024}$.

- 1: Train spinal contour detection network on $D_{spinal2023}$ and obtain initial parameters Θ^0 . Set $i \leftarrow 1$.
 - 2: **while** $V_{selected}$ is not converged **do**
 - 3: Pseudo-label samples in $D_{selected}$ using Θ^{i-1} with τ_c -based positive spinal segment instance selection.
 - 4: Update $V_{selected}$ by auto-annotation, manual-assisted annotation, and privacy review.
 - 5: $D_{SpinalAI2024} \leftarrow \{s^j | s^j \in D_{selected}, v^j = 1\}$.
 - 6: Fine-tune network from Θ^{i-1} using samples from $D_{spinal2023} \cup D_{SpinalAI2024}$, and obtain new parameters Θ^i . Set $i \leftarrow i + 1$.
 - 7: **end while**
 - 8: Return $D_{SpinalAI2024}$.
-

B. Data Engine with Dataset Generation

Our data engine is composed of iteratively four stages: pseudo-labeling, auto-annotation, manual-assisted annotation, and privacy review. Before starting the data engine, we use Stable Diffusion [21] to generate an initial set of spinal X-ray images, as shown in Algorithm 1.

1) Pseudo-Labeling: At the i -th iteration, to enable pseudo-labeling, we first train our spinal contour detection network on currently available labeled data composed of $D_{spinal2023}$ and $D_{SpinalAI2024}$, in which the trained model parameters are denoted as Θ^{i-1} . Then, we use Θ^{i-1} to label samples in $D_{selected}$. For the j -th sample s^j , the network predicts the locations of K spinal segments $[\mathbf{a}_1^j, \mathbf{a}_2^j, \dots, \mathbf{a}_K^j]$. To filter inaccurate predictions, we use a confidence threshold τ_c to select positive spinal segment instances for s^j :

$$\mathcal{A}^j = \{\mathbf{a}_k^j | p_k^j \geq \tau_c\}, \quad (9)$$

where p_k^j denotes the probability/confidence of the k -th spinal segment output by spinal contour detection network.

2) Auto-Annotation: We perform segment-level and sample-level automatic selection. We remove spinal segment instances with area smaller than 200 pixel², remove instances with illegal landmark coordinates like negative values or positions beyond image boundaries, and remove instances whose landmark coordinates cannot form a valid contour. At the sample-level, we discard samples with fewer than 10 instances, in which the average number of spinal segments per image is 17 in real datasets. We also discard samples with spinal center distances larger than three times of the average distances.

TABLE I
THE STATISTICAL CHARACTERISTICS OF DIFFERENT DATASETS.

Dataset	AASCE2019 (Public)		Spinal2023 (Private)				Spinal-AI2024 (Generated)					
	train	test	train	test	train	test	train	test				
Number of Images	481	128	700	204	16000	4000						
Height of Images (Pixel)	[973-3755]	[1159-2880]	[184-833]	[227-802]	[512-512]	[512-512]						
Width of Images (Pixel)	[355-1427]	[427-1386]	[135-457]	[147-415]	[512-512]	[512-512]						
Cobb Angle (°)	[5.96-90.0]	[8.21-80.99]	[3.22-74.26]	[5.16-67.18]	[0.0-90.0]	[0.0-90.0]						
Scoliosis Severity	Num	Avg	Num	Avg	Num	Avg	Num	Avg	Num	Avg		
Not (< 10°)	17	8.35	1	8.21	91	7.82	20	8.24	1123	8.27	278	7.86
Mild (10° - 30°)	156	21.26	37	19.88	446	17.36	130	16.69	12268	18.39	2994	18.41
Moderate (30° - 45°)	156	37.53	47	38.74	76	37.87	31	37.56	1508	35.6	369	35.76
Severe (> 45°)	152	60.89	43	56.98	87	55.87	23	56.1	1101	60.41	359	59.05

This sample-level selection can filter out samples with poor generation qualities. The index v^j of sample s^j is set to 1 in $V_{selected}$ if it is selected, and is set to 0 otherwise.

3) *Manual-Assisted Annotation*: This stage first adds annotations for samples with insufficient instances, and then manually corrects instances with inaccurate localization. We also remove non-realistic, spinal-fracture, and unclear samples.

4) *Privacy Review*: Finally, we remove generated samples with excessively high comprehensive similarity (CS) to real samples in $D_{spinal2023}$. The values of $V_{selected}$ are assigned to determine whether to discard certain samples:

$$v^j = \mathbb{1}[\max_{r=1}^{N_r} \{CS(s^j, t^r)\} \leq \tau_{CS}], \quad (10)$$

where $CS(\cdot)$ denotes CS function, t^r denotes the r -th sample in $D_{spinal2023}$, N_r is the number of samples in $D_{spinal2023}$, and τ_{CS} is a threshold. We compare s^j with all real samples so that the privacy of each real sample is preserved via τ_{CS} -based selection. To assess the degree of patient privacy leakage in spinal image generation, we introduce the definition of memorization [22]: a sample s^j is considered N_m -completely memorized if it can be extracted from the model and there are at most N_m training samples t^r in the dataset such that $CS(s^j, t^r) \leq \tau_{CS}$. Here, N_m denotes the number of nearly identical samples to s^j , which can be close to zero by setting a strict τ_{CS} value.

To measure the similarity in terms of luminance, contrast, and structural information between two images, we use structural similarity index measure (SSIM):

$$SSIM(s^j, t^r) = \frac{(2\mu_{s^j}\mu_{t^r} + c_1)(2\sigma_{s^j t^r} + c_2)}{(\mu_{s^j}^2 + \mu_{t^r}^2 + c_1)(\sigma_{s^j}^2 + \sigma_{t^r}^2 + c_2)}, \quad (11)$$

where μ_{s^j} and $\sigma_{s^j}^2$ are the mean pixel value and the variance of s^j , respectively, $\sigma_{s^j t^r}$ is the covariance of s^j and t^r , and c_1 and c_2 are constants to stabilize division by denominators. Besides, we formulate the pixel similarity (PS) between gray-scale transformed s^j and t^r with sizes $H \times W$:

$$PS(s^j, t^r) = \frac{1}{HWI} \sum_{a=1}^H \sum_{b=1}^W |GS(s^j)_{ab} - GS(t^r)_{ab}|, \quad (12)$$

where $GS(\cdot)$ denotes gray-scale transformation, and I denotes the number of gray scales (generally to be 255).

By combing Eqs. (11) and (12) using trade-off parameters λ_{ss} and λ_{ps} , we obtain the definition of CS:

$$CS(s^j, t^r) = \lambda_{ss}SSIM(s^j, t^r) + \lambda_{ps}PS(s^j, t^r). \quad (13)$$

After the above selection, we can obtain currently labeled generated dataset $D_{SpinalAI2024}$ using the selection index set $V_{selected}$. We then merge $D_{SpinalAI2024}$ with the existing $D_{spinal2023}$ to fine-tune the spinal contour detection network. We continue to generate pseudo-labels at the next iteration, and repeat this process until $V_{selected}$ converges.

IV. EXPERIMENTS

A. Datasets and Settings

1) *Datasets*: We evaluate Cobb angle measurement on public AASCE2019 [11], [60] benchmark, and our private Spinal2023 and open-source Spinal-AI2024 datasets. The dataset details are summarized in Table I.

- **AASCE2019** contains 609 frontal spine X-ray images, in which each image is annotated by clinicians with 17 spinal segments and 68 landmarks, as well as PT, MT, and TL/L Cobb angles. This dataset exhibits a wide range of image intensities and Cobb angle variations. Following the official setting [60], we use 481 images for training and 128 images for testing.
- **Spinal2023** is our private clinical dataset, which consists of 904 spine X-ray images. It is randomly split into a training set of 700 images and a test set of 204 images. A public spinal landmark detection tool [17] is utilized to annotate 68 landmarks of 17 spinal segments in each image, which are further manually checked and corrected by clinical experts. The PT, MT, and TL/L Cobb angles are calculated based on spinal landmarks. Most images have mild or moderate scoliosis, and exhibit similar image intensities.
- **SpinalAI2024** is our generated dataset with totally 20,000 spine X-ray images, in which 16,000 and 4,000 images are used for training and testing, respectively. This dataset has a broad distribution of Cobb angles with a certain range of image intensities. The annotations of spinal landmarks as well as three Cobb angles for each image is obtained by our proposed data engine.

TABLE II

COMPARISON WITH STATE-OF-THE-ART METHODS ON AASCE2019 IN TERMS OF MAXIMUM COBB ANGLE EVALUATION. THESE METHODS ARE DIVIDED INTO TRADITIONAL, REGRESSION-BASED, SEGMENTATION-BASED, AND LANDMARK-BASED METHODS, RESPECTIVELY. OUR SG-LRA CAN BE REGARDED AS COMBINING REGRESSION-BASED AND LANDMARK-BASED METHODS.

Method	SMAPE (%)
S2VR [10]	37.08
BoostNet [11]	23.44
MVC-Net [27]	35.85
Faster-RCNN [12]	25.7
MVE-Net [30]	18.95
ResNet [13]	10.81
Seg4Reg [14]	21.71
Residual U-Net [34]	16.48
TOLACT [32]	10.76
Augmented U-Net [15]	9.2
CenterNet [37]	13.46
LDNet [17]	10.81
HrNet [36]	10.03
Hourglass [16]	9.78
Linformer [38]	7.91
SG-LRA	5.05

2) *Implementation Details*: Our SG-LRA is implemented via PyTorch. Similar to previous work [20], we set the eigen-spine space dimension M and the spinal segment vertex number N to 16 and 14, respectively. The loss weights λ_{reg} and λ_{cls} in Eq. (5) are set to 0.1 and 1, respectively. We adopt stochastic gradient descent (SGD) optimizer and polynomial learning rate scheduler, with a weight decay of 0.0005, a momentum of 0.9, and an initial learning rate of 0.001. During pseudo-labeling, our spinal contour detection network is first pre-trained for 100 epochs on Spinal2023, and then are iteratively fine-tuned on training data composed of Spinal2023 images and selected generated images. The confidence threshold τ_c is set to 0.3. For privacy review, the weights λ_{ss} and λ_{ps} in Eq. (13) are set as 0.2 and 0.8, and the CS threshold τ_{CS} is set as 0.6.

3) *Evaluation Metrics*: Following the AASCE2019 [60] benchmark, we report symmetric mean absolute percentage error (SMAPE):

$$\text{SMAPE} = \frac{100\%}{N} \times \sum_{i=1}^N \left(\frac{|Cobb_{pr} - Cobb_{gt}|}{|Cobb_{pr}| + |Cobb_{gt}|} \right), \quad (14)$$

where $Cobb_{gt}$ and $Cobb_{pr}$ denote the ground-truth and predicted values, respectively. It is used to evaluate the accuracy of the maximum Cobb angle, as well as each Cobb angle of PT, MT, and TL/L. Besides, we use object detection metrics average precision (AP) and average recall (AR), as well as angle difference metric Euclidean distance (ED) to assess the effect of iterative label refinement of spinal contours.

B. Comparison with State-of-the-Art Methods

1) *Maximum Cobb Angle Evaluation*: Table II shows comparison results on the public AASCE2019 dataset. It can be seen that our SG-LRA maintains top-tier performance on AASCE2019. Compared to regression-based methods like

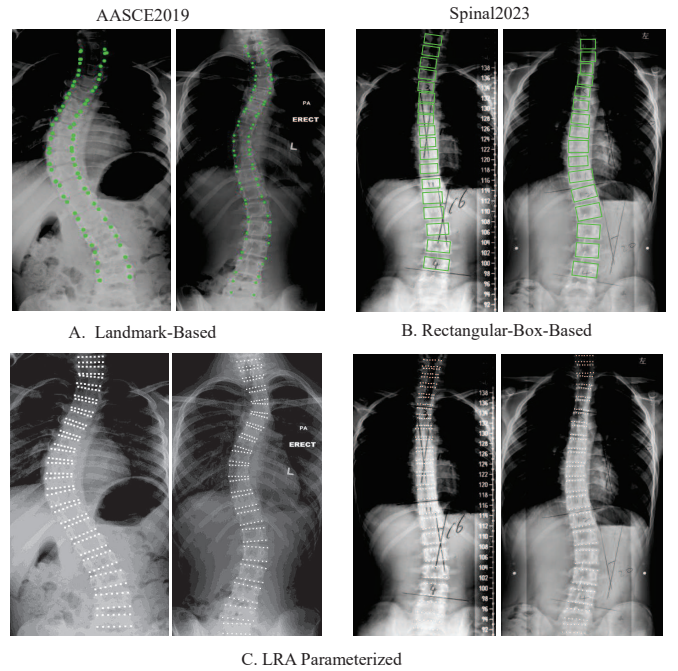


Fig. 3. Visualization of different spine representations on example images from AASCE2019 and Spinal2023.

Faster-RCNN, SG-LRA performs better, due to our LRA parameterized spine representation for precise Cobb angle calculation. Compared to segmentation-based methods, SG-LRA with sparse and dense assignments can more accurately detect spinal segment contours, better addressing issues of spinal mask connectivity/fragmentation. Compared to landmark-based methods, our LRA coefficient regression combined with the anchor box classification branch can more accurately localize corner points, giving stronger robustness for non-rectangular spinal segments.

Besides, we visualize different spine representations in Fig. 3. It can be seen that our LRA parameterized spine representation is more fine-grained than landmark-based and rectangular-box-based representations, enabling more precise Cobb angle calculation.

2) *PT, MT, and TL/L Cobb Angle Evaluation*: We conduct a more detailed comparison by evaluating Cobb angles of three regional spinal curves in Table III. Since the construction of Spinal-AI2024 involves our spinal contour detection network, the reported results of SG-LRA on Spinal-AI2024 are obtained by re-training spinal contour detection network on Spinal-AI2024. It can be observed that our SG-LRA significantly outperforms previous works in most cases.

In particular, on all the three datasets, SG-LRA performs the best on MT and TL/L Cobb angles, as well as maximum Cobb angle. This is mainly thanks to the combination of LRA coefficient regression and anchor box classification. Note that the performance for PT cure is not as good, possibly because SG-LRA focuses more on localizing irregular spinal segments rather than limiting the number of predicted spinal segments. As a result, it may involve the cervical spine in the calculation of PT Cobb angle, leading to worse results. Although previous methods fix the predicted whole scoliosis

TABLE III

SMAPE (%) RESULTS IN TERMS OF MAXIMUM COBB ANGLE AND THREE REGIONAL COBB ANGLES ON DIFFERENT DATASETS. THE RESULTS ON AASCE2019 ARE REPORTED BY LITERATURES, AND THOSE ON SPINAL2023 AND SPINAL-AI2024 ARE IMPLEMENTED USING THEIR CODE.

Method	AASCE2019 (Public)				Spinal2023 (Private)				Spinal-AI2024 (Generated)			
	Max	PT	MT	TL/L	Max	PT	MT	TL/L	Max	PT	MT	TL/L
LDNet	10.81	6.26	18.04	23.42	17.22	23.88	24.12	32.62	15.23	32.68	21.1	27.57
Hourglass	9.78	11.13	15.22	21.03	16.05	21.63	26.67	24.5	10.25	26.8	18.6	20.02
Residual U-Net	16.48	9.71	25.97	33.01	24.3	16.6	31.2	35.4	13.3	10.79	19.93	38.18
Linformer	7.91	4.86	14.65	20.49	19.1	17.25	21.17	29.17	11.59	7.83	18.82	24.62
SG-LRA	5.05	12.48	6.27	14.04	7.13	23.3	9.49	17.25	5.34	22.91	8.64	16.69

TABLE IV

MAXIMUM COBB ANGLE ESTIMATION RESULTS OF DIFFERENT VARIANTS OF OUR SPINAL CONTOUR DETECTION NETWORK ON SPINAL2023.

C_{sparse} , C_{dense} , R_{sparse} , AND R_{dense} DENOTES SPARSE ASSIGNMENT AND DENSE ASSIGNMENT IN THE CLASSIFICATION AND REGRESSION BRANCHES, RESPECTIVELY.

C_{sparse}	C_{dense}	R_{sparse}	R_{dense}	SMAPE(%)
✓	✓			61.03
✓		✓	✓	53.97
	✓		✓	25.02
✓	✓	✓	✓	7.13

to 17 spinal segments, which often obtains more accurate PT predictions, complex pre-processing of data and annotations based on clinical knowledge are required.

It can be seen that segmentation-based method Residual U-Net achieves the best PT Cobb angle estimation result on Spinal2023, and landmark-based method Linformer achieves the best PT Cobb angle estimation result on Spinal-AI2024. We notice that Spinal2023 has limited images while Spinal-AI2024 has a larger scale. In this case, landmark-based methods suffer from insufficient training data on Spinal2023 but can be trained well on Spinal-AI2024, while segmentation-based methods have larger advantages on Spinal2023 with smaller scale. In contrast, our SG-LRA consistently works well across small and large datasets.

C. Ablation study

In this section, we evaluate the key modules in our framework: spinal contour detection network and data engine.

1) *Spinal Contour Detection Network*: Our spinal contour detection network consists of LRA coefficient regression branch and anchor box classification branch, with each branch containing sparse and dense assignments. Table IV presents the results of different variants on Spinal2023.

Regression and Classification Branches. We can see that using classification or regression branches alone both perform poor, in which the regression is more important. When combining both regression and classification, our full spinal contour detection network achieves the smallest SMAPE.

Sparse and Dense Assignments. In the case of combining both branches, only utilizing sparse or dense assignments still cannot achieve the desired Cobb angle measurement

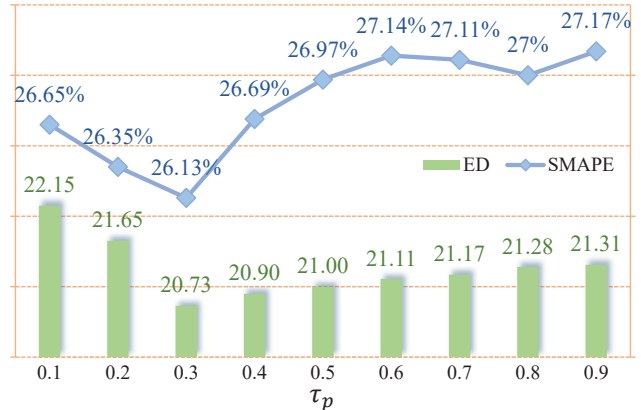


Fig. 4. Performance of our spinal contour detection network under different confidence thresholds on generated dataset obtained at the first data engine iteration. Note that when τ_c is set optimally at 0.3, ED and SMAPE results on the final Spinal-AI2024 dataset will be increased from 20.73 and 26.13% to 6.23 and 5.34%, respectively.

effect. Due to more fine-grained prediction, the use of dense assignment has a higher accuracy than sparse assignment.

2) *Data Engine*: During our framework, the X-ray images generated by Stable Diffusion [21] have a certain degree of noises, in which some severe noises do not conform to reality. This problem is widespread in medical image generation, due to the distribution characteristics of training data itself, including the lack of rare cases like Cobb angles greater than 45 degrees. Our data engine is proposed to solve this issue, and is validated in this section.

Different Confidence Thresholds. To investigate the effects of different confidence thresholds, we train spinal contour detection network on $D_{SpinalAI2024}$ obtained at the first data engine iteration using different τ_c with a interval of 0.1, as illustrated in Fig. 4. The results show that setting τ_c to 0.3 results in the highest pseudo-label qualities. When τ_c is lower, the selected spinal segment instances may contain more noises, which complicates the further denoising process. When τ_c is higher, important positive instances may be missing, causing large errors in calculating Cobb angles.

Denoising in Auto- and Manual-Assisted Annotation. Table V shows the results before and after denoising, in which AP and AR are calculated between current labels and the labels in the final Spinal-AI2024. It is indicated that denoising significantly improves the qualities of pseudo labels.

Different Sample Selection Strategies. We conduct three experiments using different sample selection strategies, as

TABLE V

AP AND AR RESULTS ON SIX SUBSETS OF SPINAL-AI2024 BEFORE AND AFTER DENOISING AT THE FIRST DATA ENGINE ITERATION.

Subset	AP		AR	
	Before	After (\uparrow)	Before	After (\uparrow)
1	60.5	79.8 (19.3)	15.9	20.8 (4.9)
2	80.1	89.9 (9.8)	20.9	26.3 (5.4)
3	89.6	94.1 (4.5)	26.3	32.9 (6.6)
4	95.2	96.5 (1.3)	33.0	39.8 (6.8)
5	94.1	95.5 (1.4)	32.9	38.8 (5.9)
6	95.6	96.6 (1.0)	39.0	45.9 (6.9)

TABLE VI

RESULTS USING DIFFERENT SELECTIONS ON SPINAL-AI2024 FROM THE FIRST TO THE SIX ITERATIONS. "NO", "INDEP.", AND "CUMUL." DENOTE NO FILTERING, AND UPDATING $V_{selected}$ IN INDEPENDENT AND CUMULATIVE WAYS ACROSS ITERATIONS, RESPECTIVELY.

	Selection	1	2	3	4	5	6
AP	No	84.0	87.9	95.3	96.4	96.6	94.8
	Indep.	84.3	88.1	95.5	96.5	96.6	96.7
	Cumul.	84.3	89.2	95.6	96.6	97.8	96.9
AR	No	26.0	32.1	38.8	45.5	56.1	72.8
	Indep.	26.1	31.8	38.8	45.6	56.2	74.3
	Cumul.	26.1	32.0	38.8	45.6	56.2	74.4

shown in Table VI. If a sample is filtered and will not be selected in the next iterations, i.e. cumulative way, the overall highest quality improvement can be achieved. If $V_{selected}$ is updated independently across iterations, the quality improvement becomes worse but is still better than no filtering. This demonstrates the cumulative effectiveness of combined denoising and privacy review processes.

We also present the filtered spinal segment instances and unreasonable samples during sample selection in Fig. 5. It can be seen inaccurate pseudo-labels and poor generated samples are discarded.

V. AI RESPONSIBILITY AND ETHICAL STANDARDS

The aim of this research is to enhance the accuracy and safety of automatic Cobb angle measurement for scoliosis diagnosis. Careful data scrutiny and adherence to ethical standards are crucial when introducing this technology. A thorough privacy review of the AI-generated data is necessary to protect patient information and rights. Upholding the highest ethical principles is a fundamental responsibility for researchers in this domain.

A. Data Availability

The datasets used in this paper include the public AASCE2019 benchmark, our private Spinal2023 dataset, and our generated Spinal-AI2024 dataset. Spinal-AI2024 has been released at <https://github.com/Ernestchenchen/Spinal-AI2024>. Although Spinal2023 can not be made publicly available due to patient privacy, this paper has provided many details regarding the data source, data processing, and data distribution. Besides, Spinal2023 is granted under a strict data usage agreement and is approved by the institutional Medical

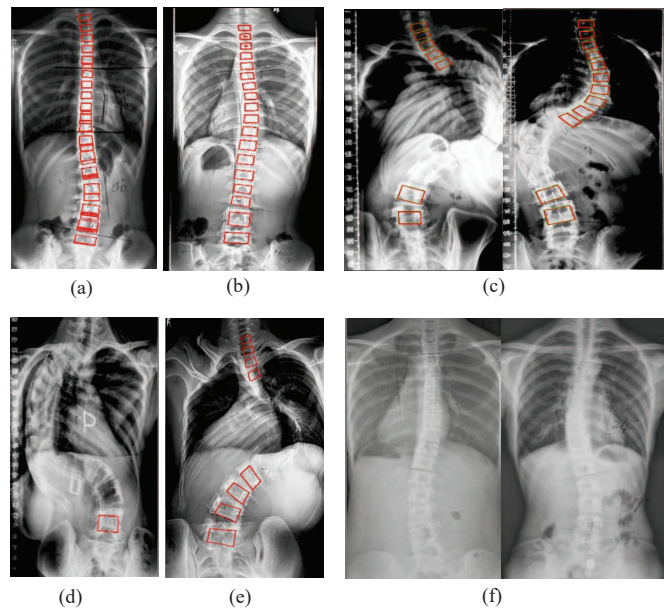


Fig. 5. Illustration of discarded spinal segment instances as well as unreasonable samples during sample selection. (a) Inaccurate spinal segment instances due to low threshold; (b) Spinal segment instances with area smaller than 200 pixel²; (c) Samples with fewer than 10 instances; (d) Image distortion; (e) Spinal fracture; (f) Samples with excessively high comprehensive similarity (CS).

Research Ethics Committee. Spinal-AI2024 conducts privacy assessments to prevent patient re-identification.

B. Data Ethics

1) *Public AASCE2019*: The use of this benchmark dataset allows objective evaluation and comparison of our automatic Cobb angle measurement techniques. Importantly, the AASCE dataset has undergone appropriate anonymization and de-identification to protect patient privacy, in alignment with relevant ethical guidelines and regulations.

2) *Private Spinal2023*: In addition to the public AASCE dataset, this research also utilized the private Spinal2023 dataset, which contains X-ray images and Cobb angle annotations for a larger scoliosis patient cohort. Access to Spinal2023 was granted under a strict data usage agreement with comprehensive privacy and protection protocols, reviewed and approved by the institutional Medical Research Ethics Committee.

3) *Generated Spinal-AI2024*: This dataset was created by training generative AI models on Spinal2023 to synthesize additional X-ray images and Cobb angle annotations. The research team carefully reviewed and validated the Spinal-AI2024 dataset to ensure it preserves the original data characteristics.

The inclusion of the Spinal-AI2024 dataset expands the training and evaluation data, which can enhance the robustness and generalizability of the automatic Cobb angle measurement algorithms. However, the use of AI-generated data requires additional ethical considerations. We have implemented rigorous data provenance tracking, algorithmic transparency, and human oversight to verify the Spinal-AI2024 dataset's integrity

TABLE VII

IMAGE SIMILARITY REVIEW CHECKLIST (EXCERPT). “NEW IMAGE” DENOTES IMAGES FROM THE GENERATED DATASET SPINAL-AI2024, “TOP k -IMAGE” DENOTES THE IMAGE IN THE k -TH PLACE OF DESCENDING SIMILARITY IN THE PRIVATE DATASET SPINAL2023, AND “ACS” DENOTES THE AVERAGE OF TOP1-CS, TOP2-CS, AND TOP3-CS.

New Image	Top1-Image	Top1-SSIM	...	Top1-Image	Top1-PS	...	Top1-CS	Top2-CS	Top3-CS	ACS
000001.jpg	000196.png	38.24	...	000290.png	37.78	...	47.61	47.15	46.77	47.18
...
001257.jpg	000527.png	52.76	...	000427.png	88.58	...	59.92	58.18	58.01	58.71
...
020140.jpg	000009.png	44.2	...	000531.png	89.3	...	53.22	53.15	52.83	53.07
...
020000.jpg	000763.png	34.46	...	000493.png	82.25	...	44.02	43.91	43.88	43.93

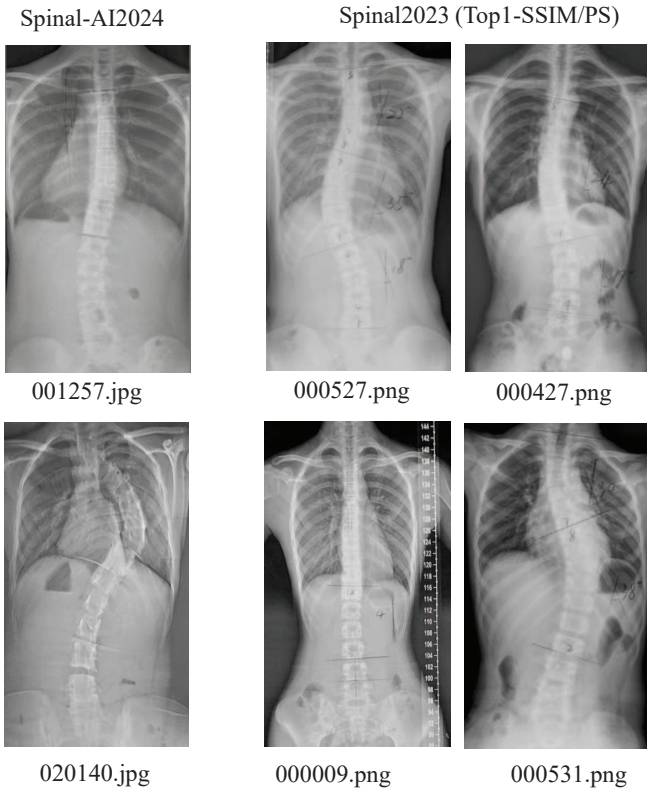


Fig. 6. Illustration of highest similar images.

and fidelity. Comprehensive privacy assessments have also been conducted to prevent potential patient re-identification.

For each Spinal-AI2024 image, a top-3 comprehensive similarity review is presented in Table VII, in which the most similar images are shown in Fig. 6. The results show that our generated dataset has distorted the original annotations and produced spinal curvature variations, which can prevent excessive patient information leakage.

VI. CONCLUSION

We have proposed a novel self-generating framework utilizing LRA parameterized spine representation for automatic Cobb angle measurement. LRA coefficient regression and anchor box classification with sparse and dense assignments are combined to detect irregular contours of spinal segments.

Besides, we have proposed a data engine with semi-supervised labeling and privacy review, which culminates in the open-source largest scoliosis X-ray dataset Spinal-AI2024. Extensive experiments have demonstrated the effectiveness of our method, achieving state-of-the-art performance on public, private, and generated datasets for both maximum Cobb angle and three regional Cobb angles.

REFERENCES

- [1] C. Du, J. Yu, J. Zhang, J. Jiang, H. Lai, W. Liu, Y. Liu, H. Li, and P. Wang, “Relevant areas of functioning in patients with adolescent idiopathic scoliosis on the international classification of functioning, disability and health: The patients’ perspective.” *Journal of Rehabilitation Medicine*, vol. 48, no. 9, pp. 806–814, 2016.
- [2] C. Lang, R. Wang, Z. Chen, S. He, Q. Zou, J. Wu, and X. Zhu, “Incidence and risk factors of cardiac abnormalities in patients with idiopathic scoliosis,” *World Neurosurgery*, vol. 125, pp. e824–e828, 2019.
- [3] X. Zhu, R. Chen, Z. Shao, M. Zhang, Y. Dai, W. Zhang, and C. Lang, “Mgscoliosis: Multi-grained scoliosis detection with joint ordinal regression from natural image,” *Alexandria Engineering Journal*, vol. 111, pp. 329–340, 2025.
- [4] G. Prabhu, “Automatic quantification of spinal curvature in scoliotic radiograph using image processing,” *Journal of Medical Systems*, vol. 36, no. 3, pp. 1943–1951, 2012.
- [5] P. Scholten and A. Veldhuizen, “Analysis of cobb angle measurements in scoliosis,” *Clinical Biomechanics*, vol. 2, no. 1, pp. 7–13, 1987.
- [6] C. B. McLeod, “Anesthesia for pediatric spinal deformity,” in *Multidisciplinary Spine Care*. Springer, 2022, pp. 667–710.
- [7] T. Vrtovec, F. Pernuš, and B. Likar, “A review of methods for quantitative evaluation of spinal curvature,” *European Spine Journal*, vol. 18, pp. 593–607, 2009.
- [8] J. Pruijs, M. Hageman, W. Keessen, R. Van Der Meer, and J. Van Wieringen, “Variation in cobb angle measurements in scoliosis,” *Skeletal Radiology*, vol. 23, pp. 517–520, 1994.
- [9] Y. Sun, Y. Xing, Z. Zhao, X. Meng, G. Xu, and Y. Hai, “Comparison of manual versus automated measurement of cobb angle in idiopathic scoliosis based on a deep learning keypoint detection technology,” *European Spine Journal*, pp. 1–10, 2022.
- [10] H. Sun, X. Zhen, C. Bailey, P. Rasoulinejad, Y. Yin, and S. Li, “Direct estimation of spinal cobb angles by structured multi-output regression,” in *International Conference on Information Processing in Medical Imaging*. Springer, 2017, pp. 529–540.
- [11] H. Wu, C. Bailey, P. Rasoulinejad, and S. Li, “Automatic landmark estimation for adolescent idiopathic scoliosis assessment using boostnet,” in *International Conference on Medical Image Computing and Computer Assisted Intervention*. Springer, 2017, pp. 127–135.
- [12] B. Khanal, L. Dahal, P. Adhikari, and B. Khanal, “Automatic cobb angle detection using vertebra detector and vertebra corners regression,” in *Computational Methods and Clinical Applications for Spine Imaging*. Springer, 2020, pp. 81–87.
- [13] S. Targ, D. Almeida, and K. Lyman, “Resnet in resnet: Generalizing residual architectures,” in *International Conference on Learning Representations Workshops*, 2016.

- [14] Y. Lin, H.-Y. Zhou, K. Ma, X. Yang, and Y. Zheng, "Seg4reg networks for automated spinal curvature estimation," in *Computational Methods and Clinical Applications for Spine Imaging*. Springer, 2020, pp. 69–74.
- [15] Y. Wu, K. Namdar, C. Chen, S. Hosseinpour, M. Shroff, A. S. Doria, and F. Khalvati, "Automated adolescence scoliosis detection using augmented u-net with non-square kernels," *Canadian Association of Radiologists Journal*, vol. 74, no. 4, pp. 667–675, 2023.
- [16] T. Xu and W. Takano, "Graph stacked hourglass networks for 3d human pose estimation," in *IEEE Conference on Computer Vision and Pattern Recognition*. IEEE, 2021, pp. 16 105–16 114.
- [17] J. Yi, P. Wu, Q. Huang, H. Qu, and D. N. Metaxas, "Vertebra-focused landmark detection for scoliosis assessment," in *IEEE International Symposium on Biomedical Imaging*. IEEE, 2020, pp. 736–740.
- [18] Z. Shao, Z. Liu, J. Cai, and L. Ma, "Jaa-net: Joint facial action unit detection and face alignment via adaptive attention," *International Journal of Computer Vision*, vol. 129, no. 2, pp. 321–340, 2021.
- [19] W. Park, D. Jin, and C.-S. Kim, "Eigencontours: Novel contour descriptors based on low-rank approximation," in *IEEE Conference on Computer Vision and Pattern Recognition*. IEEE, 2022, pp. 2667–2675.
- [20] Y. Su, Z. Chen, Z. Shao, Y. Du, Z. Ji, J. Bai, Y. Zhou, and Y.-G. Jiang, "Lranet: Towards accurate and efficient scene text detection with low-rank approximation network," in *AAAI Conference on Artificial Intelligence*, 2024, pp. 4979–4987.
- [21] R. Rombach, A. Blattmann, D. Lorenz, P. Esser, and B. Ommer, "High-resolution image synthesis with latent diffusion models," in *IEEE Conference on Computer Vision and Pattern Recognition*. IEEE, 2022, pp. 10 684–10 695.
- [22] N. Carlini, J. Hayes, M. Nasr, M. Jagielski, V. Shwag, F. Tramèr, B. Balle, D. Ippolito, and E. Wallace, "Extracting training data from diffusion models," in *USENIX Security Symposium*, 2023, pp. 5253–5270.
- [23] K. Packhäuser, L. Folle, F. Thamm, and A. Maier, "Generation of anonymous chest radiographs using latent diffusion models for training thoracic abnormality classification systems," in *IEEE International Symposium on Biomedical Imaging (ISBI)*. IEEE, 2023, pp. 1–5.
- [24] M. N. Rizve, K. Duarte, Y. S. Rawat, and M. Shah, "In defense of pseudo-labeling: An uncertainty-aware pseudo-label selection framework for semi-supervised learning," *International Conference on Learning Representations*, 2021.
- [25] A. Kirillov, E. Mintun, N. Ravi, H. Mao, C. Rolland, L. Gustafson, T. Xiao, S. Whitehead, A. C. Berg, W.-Y. Lo *et al.*, "Segment anything," in *IEEE International Conference on Computer Vision*. IEEE, 2023, pp. 4015–4026.
- [26] W. Xue, A. Islam, M. Bhaduri, and S. Li, "Direct multitype cardiac indices estimation via joint representation and regression learning," *IEEE Transactions on Medical Imaging*, vol. 36, no. 10, pp. 2057–2067, 2017.
- [27] H. Wu, C. Bailey, P. Rasoulinejad, and S. Li, "Automated comprehensive adolescent idiopathic scoliosis assessment using mvc-net," *Medical Image Analysis*, vol. 48, pp. 1–11, 2018.
- [28] Z. Shao, H. Zhu, J. Tang, X. Lu, and L. Ma, "Explicit facial expression transfer via fine-grained representations," *IEEE Transactions on Image Processing*, vol. 30, pp. 4610–4621, 2021.
- [29] Z. Shao, Y. Zhou, J. Cai, H. Zhu, and R. Yao, "Facial action unit detection via adaptive attention and relation," *IEEE Transactions on Image Processing*, vol. 32, pp. 3354–3366, 2023.
- [30] L. Wang, Q. Xu, S. Leung, J. Chung, B. Chen, and S. Li, "Accurate automated cobb angles estimation using multi-view extrapolation net," *Medical Image Analysis*, vol. 58, p. 101542, 2019.
- [31] Y. Pan, Q. Chen, T. Chen, H. Wang, X. Zhu, Z. Fang, and Y. Lu, "Evaluation of a computer-aided method for measuring the cobb angle on chest x-rays," *European Spine Journal*, vol. 28, pp. 3035–3043, 2019.
- [32] C. Chen, K. Namdar, Y. Wu, S. Hosseinpour, M. Shroff, A. S. Doria, and F. Khalvati, "Automating cobb angle measurement for adolescent idiopathic scoliosis using instance segmentation," *arXiv preprint arXiv:2211.14122*, 2022.
- [33] O. Ronneberger, P. Fischer, and T. Brox, "U-net: Convolutional networks for biomedical image segmentation," in *International Conference on Medical Image Computing and Computer Assisted Intervention*. Springer, 2015, pp. 234–241.
- [34] M.-H. Horng, C.-P. Kuok, M.-J. Fu, C.-J. Lin, and Y.-N. Sun, "Cobb angle measurement of spine from x-ray images using convolutional neural network," *Computational and Mathematical Methods in Medicine*, vol. 2019, no. 1, p. 6357171, 2019.
- [35] G. V. Pednekar, J. K. Udupa, D. J. McLaughlin, X. Wu, Y. Tong, C. B. Simone II, J. Camaratta, and D. A. Torigian, "Image quality and segmentation," in *Medical Imaging: Image-Guided Procedures, Robotic Interventions, and Modeling*, vol. 10576. SPIE, 2018, pp. 622–628.
- [36] K. Sun, B. Xiao, D. Liu, and J. Wang, "Deep high-resolution representation learning for human pose estimation," in *IEEE Conference on Computer Vision and Pattern Recognition*. IEEE, 2019, pp. 5693–5703.
- [37] Z. Zhou, J. Zhu, and C. Yao, "Vertebral center points locating and cobb angle measurement based on deep learning," *Applied Sciences*, vol. 13, no. 6, p. 3817, 2023.
- [38] Y. Guo, Y. Li, H. Song, W. He, and K. Yuan, "Cobb angle rectification with dual-activated linformer," in *IEEE International Conference on Mechatronics and Automation*. IEEE, 2022, pp. 1003–1008.
- [39] S. Kazemini, C. Baur, A. Kuijper, B. van Ginneken, N. Navab, S. Al-barqouni, and A. Mukhopadhyay, "Gans for medical image analysis," *Artificial Intelligence in Medicine*, vol. 109, p. 101938, 2020.
- [40] A. Tucker, Z. Wang, Y. Rotalinti, and P. Myles, "Generating high-fidelity synthetic patient data for assessing machine learning healthcare software," *NPJ Digital Medicine*, vol. 3, no. 1, pp. 1–13, 2020.
- [41] A. A. A. Setio, F. Ciompi, G. Litjens, P. Gerke, C. Jacobs, S. J. Van Riel, M. M. W. Wille, M. Naqibullah, C. I. Sánchez, and B. Van Ginneken, "Pulmonary nodule detection in ct images: False positive reduction using multi-view convolutional networks," *IEEE Transactions on Medical Imaging*, vol. 35, no. 5, pp. 1160–1169, 2016.
- [42] N. Patki, R. Wedge, and K. Veeramachaneni, "The synthetic data vault," in *IEEE International Conference on Data Science and Advanced Analytics*. IEEE, 2016, pp. 399–410.
- [43] T. Karras, "Progressive growing of gans for improved quality, stability, and variation," *arXiv preprint arXiv:1710.10196*, 2017.
- [44] I. Goodfellow, J. Pouget-Abadie, M. Mirza, B. Xu, D. Warde-Farley, S. Ozair, A. Courville, and Y. Bengio, "Generative adversarial networks," *Communications of the ACM*, vol. 63, no. 11, pp. 139–144, 2020.
- [45] L. Mescheder, S. Nowozin, and A. Geiger, "The numerics of gans," *Advances in Neural Information Processing Systems*, vol. 30, 2017.
- [46] T. Karras, S. Laine, M. Aittala, J. Hellsten, J. Lehtinen, and T. Aila, "Analyzing and improving the image quality of stylegan," in *IEEE Conference on Computer Vision and Pattern Recognition*. IEEE, 2020, pp. 8110–8119.
- [47] A. Brock, "Large scale gan training for high fidelity natural image synthesis," *arXiv preprint arXiv:1809.11096*, 2018.
- [48] B. Lo, "Sharing clinical trial data: Maximizing benefits, minimizing risk," *Jama*, vol. 313, no. 8, pp. 793–794, 2015.
- [49] A. Esteva, A. Robicquet, B. Ramsundar, V. Kuleshov, M. DePristo, K. Chou, C. Cui, G. Corrado, S. Thrun, and J. Dean, "A guide to deep learning in healthcare," *Nature Medicine*, vol. 25, no. 1, pp. 24–29, 2019.
- [50] S. Honari, P. Molchanov, S. Tyree, P. Vincent, C. Pal, and J. Kautz, "Improving landmark localization with semi-supervised learning," in *IEEE Conference on Computer Vision and Pattern Recognition*. IEEE, 2018, pp. 1546–1555.
- [51] O. Moskvyyak, F. Maire, F. Dayoub, and M. Baktashmotlagh, "Semi-supervised keypoint localization," *arXiv preprint arXiv:2101.07988*, 2021.
- [52] C. Li and G. H. Lee, "From synthetic to real: Unsupervised domain adaptation for animal pose estimation," in *IEEE Conference on Computer Vision and Pattern Recognition*. IEEE, 2021, pp. 1482–1491.
- [53] W. Shi, Y. Gong, C. Ding, Z. M. Tao, and N. Zheng, "Transductive semi-supervised deep learning using min-max features," in *European Conference on Computer Vision*, 2018, pp. 299–315.
- [54] K. Yi and J. Wu, "Probabilistic end-to-end noise correction for learning with noisy labels," in *IEEE Conference on Computer Vision and Pattern Recognition*. IEEE, 2019, pp. 7017–7025.
- [55] G.-H. Wang and J. Wu, "Repetitive prediction deep decipher for semi-supervised learning," in *AAAI Conference on Artificial Intelligence*, 2020, pp. 6170–6177.
- [56] Q. Xie, M.-T. Luong, E. Hovy, and Q. V. Le, "Self-training with noisy student improves imagenet classification," in *IEEE Conference on Computer Vision and Pattern Recognition*. IEEE, 2020, pp. 10 687–10 698.
- [57] K. He, X. Zhang, S. Ren, and J. Sun, "Deep residual learning for image recognition," in *IEEE Conference on Computer Vision and Pattern Recognition*. IEEE, 2016, pp. 770–778.
- [58] T.-Y. Lin, P. Dollár, R. Girshick, K. He, B. Hariharan, and S. Belongie, "Feature pyramid networks for object detection," in *IEEE Conference on Computer Vision and Pattern Recognition*. IEEE, 2017, pp. 2117–2125.
- [59] A. Blum, J. Hopcroft, and R. Kannan, *Foundations of Data Science*. Cambridge University Press, 2020.
- [60] L. Wang, C. Xie, Y. Lin, H.-Y. Zhou, K. Chen, D. Cheng, F. Dubost, B. Collety, B. Khanal, B. Khanal *et al.*, "Evaluation and comparison of accurate automated spinal curvature estimation algorithms with spinal anterior-posterior x-ray images: The aasce2019 challenge," *Medical Image Analysis*, vol. 72, p. 102115, 2021.